Twisted light Michelson interferometer for high precision refractive index measurements

NICOLA M. KERSCHBAUMER,[1,3,4] LUCAS I. FOCHLER,[1,3]
MICHAEL REICHENSPURNER,[1] SEBASTIAN RIEGER,[1]
MICHAEL FEDORUK,[2] JOCHEN FELDMANN,[1]
AND THEOBALD LOHMÜLLER[1,5]

[1]*Chair for Photonics and Optoelectronics, Nano-Institute Munich, Department of Physics,
Ludwig-Maximilians-Universität (LMU), Königinstraße 10, 80539 Munich, Germany*
[2]*Vortex Photonics, Hubertusstr. 11, 82152 Planegg, Germany*
[3]*Equal contributors.*
[4]*nicola.kerschbaumer@lmu.de*
[5]*t.lohmueller@lmu.de*

Abstract: Using orbital angular momentum beams in a Michelson interferometer opens the possibility for non-invasive measurements of refractive index changes down to 10^{-6} refractive index units. We demonstrate the application of a twisted light interferometer to directly measure the concentration of NaCl and glucose solutions label-free and *in situ* and to monitor temperature differences in the mK-µK range. From these measurements we can extract a correlation of the refractive index to concentration and to temperature from a liquid sample which is in good agreement with literature. Applying this type of twisted light interferometry yields a novel, robust, and easily implementable method for *in situ* monitoring of concentration and temperature changes in microfluidic samples.

1. Introduction

Michelson interferometry has been invented more than a century ago and has since been developed from the basic principle [1] to high end technical applications which have most recently enabled the detection of gravitational waves [2,3]. Technical advances to improve the resolution, for example for displacement measurements, include the development of heterodyne interferometers with 10 pm accuracy [4], homodyne interferometers resolving sub-picometer distances [5,6], increasing the optical path length [5] or modulations of the signal [7]. This list is by far not exhaustive but demonstrates the significant creativity that has been applied to improve this technique to enhance the measurement power for multiple applications. However, obtaining high resolution typically requires a significant amount of complex signal processing or added components and a very precise control of the experimental conditions [8].

A novel twist to perform interferometry has been introduced by alternating the mode of the incoming light source. Emile and Emile [9] have reported on an innovative way to perform distance measurements by Michelson interferometry with Laguerre-Gauss (LG) beams containing orbital angular momentum (OAM). An OAM beam has a helical wave front and a central phase singularity [10–12]. It is important to note that the orientation of the electromagnetic field is rotating and this is not a polarization effect. The photons carry orbital angular momentum [12] and thereby give the beam a screw-like shape resulting in a LG or so-called doughnut mode [13]. The number of windings intertwined with themselves is referred to as the topological charge m_l of the beam [14]. This topological charge carries a sign which describes the direction the beam is twisted in, also referred to as the helicity. OAM beams are applied in various fields such as stimulated emission depletion (STED) super-resolution microscopy [15] and are highly

investigated [16,17]. OAM beams can be engineered in various forms [17–19] but their use for high-resolution interferometry is largely unexplored.

When two OAM beams with opposing helicity interfere, the resulting pattern resembles a daisy flower, where the number of petals is twice the topological charge [9,20–23]. A phase shift between the interferometer beam paths (by changing the optical length or the medium in the beam path) results in a rotation of the flower pattern in the azimuthal plane. The rotation can be quantified by using a charged coupled device (CCD) camera. So far, OAM interferometry has been applied in the lab to measure displacement [9,24], rotation [23,25] and its potential has been discussed theoretically in multiple studies [26–28], including for the possible enhancement in gravitational wave detection [29,30]. Emile and Emile [9] reported on OAM interferometry for length difference measurements and predicted a possible resolution of 44 pm. Later, Verma and Yadav [26] proposed how a resolution of 3 pm could be theoretically achieved. This is only one order of magnitude less sensitive compared to the resolution reached by high-end interferometers [5] and thereby shows the great potential this relatively new approach can provide. It should be noted that general limitations such as, for example, phase noise that apply to all interferometers also apply to OAM interferometry and may even have a larger impact. These conceptual limitations must be considered when comparing the potentially achievable performance of OAM interferometry with high-end interferometers that employ sophisticated measures to improve their resolution. However, our new approach bears the advantage that it offers a very simple and inexpensive way to conduct very sensitive measurements of liquids in a normal laboratory setting without relying on complex equipment such as vacuum chambers, spectrometers, clean-room conditions or signal post-processing.

Motivated by the reports by Emile and Verma, we have applied OAM interferometry to measure concentration or temperature changes of liquid samples. Both temperature and concentration of a solution have an influence on its refractive index [31–33], which in turn causes a phase shift that can be measured by interferometry. For biochemical applications, it is desirable to monitor small variations in concentration [34] or temperature non-invasively, which is also true for many chemical reactions or pharmaceutical production processes [35]. Concentration measurements are commonly performed, for example, with electrochemical or spectroscopical means. The best suited technique is thereby often dependent on the type of analyte. Optical approaches are desirable to perform label-free, high precision measurements of concentration or temperature, in particular for microfluidic or lab-on-a-chip applications, where *in situ* monitoring of concentration gradients or temperature variances often presents a challenge. For large molecules, such as DNA or proteins, concentrations can be measured in the nM range by absorption but for smaller, uncharged particles this is not always feasible. Indeed, interferometric approaches have been developed to perform concentration or temperature measurements [36] including measuring fringes of monochromatic order [37], fringe shifts [38], or a phase-modulation [39]. These *in situ* concentration measurements achieved sensitivities of refractive index unit (RIU) changes between the order of 10^{-5} [37] and 10^{-8} [39]. Several more approaches can be found in literature [40–48], including refractometry [49–52] with lower or similar resolutions. We perform measurements for aqueous solutions containing NaCl or glucose and show that it is possible to measure micromolar or 10^{-4} w% concentrations, independent of the character of the analyte. Specifically for glucose, we are able to measure label-free in the micromolar range, which is challenging to achieve with other methods [53].

2. Materials and methods

The OAM interferometer system is set up on an air-balanced laser table (*Melles Griot*, USA). A Verdi V10 10 W laser (*Coherent,* USA) with $\lambda = 532$ nm was operated at 50 mW for all measurements. The laser power was kept constant in all of our measurements to avoid refractive index variations due to non-linear effects. Additionally, temperature control measurements were

performed with a highly sensitive IR camera to exclude any undesired sample heating by the laser beam. Standard laser mirrors (*Thorlabs*, USA) are used to guide the laser beams. A 50–50 beam splitter (*Thorlabs*, USA) is used to split the beam. The entire interferometer is encapsulated in an acrylic glass box (*Thorlabs*, USA) to avoid external disturbances, especially air flow and temperature fluctuations. For the concentration measurements, the flow cell is filled with ddH$_2$O. Then a syringe pump (*TSE Systems GmbH*, Germany) slowly pumps through a NaCl or glucose aqueous solution at a rate of 0.9 ml/min. 1 mL is pumped through the flow cell to ensure complete liquid exchange, also considering the connecting tubes. After each measurement the flow cell is thoroughly rinsed and filled with ddH$_2$O again. The NaCl and glucose solutions are prepared using ddH$_2$O and pure NaCl and D-glucose (*Sigma Aldrich*, USA) without further purification. Control measurements are performed using a UV-VIS absorption spectrometer Cary 5000 (*Agilent Technologies*, USA). For the temperature measurement ddH$_2$O is heated up in a heat bath and injected into a flow cell to cool down to room temperature. An infrared camera (*FLIR Systems*, USA, AC655, 20 mK resolution) is used for control measurements of the flow cell temperature.

3. OAM interferometer

We present an optical, contactless method to measure 10^{-6} refractive index unit (RIU) changes of a liquid in a flow cell and temperature changes in the single mK range. To this end, we built an interferometer based on interference of OAM beams. We realize OAM beams using spiral phase plates (SPPs) (*Vortex Photonics*, Germany). The general working principle of a SPP is demonstrated in Fig. 1(a). The SPP consists of fused silica and has an increasing thickness $h_s(\theta)$ depending on the azimuthal angle θ. We use spiral phase plates with 64 steps for an incoming laser (continuous wave, $\lambda = 532$ nm) with $m_l = 3$ or $m_l = 6$. SPPs are composed of individual steps and not a continuous smooth surface, due to resolution limits in manufacturing. However, for a step number higher than 32, the conversion efficiency is comparable to a smooth surface [54,55]. Therefore, 32 is the minimum number of steps required for the SPP to not affect the measurement accuracy. The SPP depicted in Fig. 1(a) has one section shifting the phase from 0 to 2π, meaning it generates OAM beams with a topological charge $m_l = 1$. This value can be any integer. The phase shift ϕ experienced by the beam is dependent on the wavelength of the incoming beam λ, the refractive index of the SPP n_{SPP} as well as the refractive index of the surrounding medium n_0, the azimuthal angle θ, the lowest height h_0 and the maximum height h_s of the SPP [56]:

$$\phi(\theta, \lambda) = \frac{2\pi}{\lambda} \left(\frac{(n_{SPP} - n_0)h_s\theta}{2\pi} + n_{SPP}h_0 \right). \tag{1}$$

An incident laser beam with the respective wavelength and a Gaussian mode profile is transformed into a beam with a Laguerre-Gaussian mode profile when transversing the SPP. Images of the simulated mode profiles are displayed next to the respective beams in Fig. 1(a). A schematic of the interferometer setup is shown in Fig. 1(b). The cross-section of the incoming beam is enlarged by a beam expander to fully illuminate the SPP. The beam is then split by a 50–50 beam splitter (BS) into two arms. In one arm, a cylindrical lens is placed to invert the OAM beam helicity. The resulting beam rotates in the opposing direction and the topological charge changes in sign to -m_l. It should be noted that the use of a cylindrical lens is not mandatory to invert helicity and the lens could be replaced by other optical tools such as a dove prism or a right-angle prism. Furthermore, other interferometer arrangements are possible, including Mach-Zehnder configurations, where also the sign and magnitude of the topological charge of OAM beams can be determined by self-referenced interference [57,58].

A flow cell that allows for liquid exchange during the measurement is placed in the other interferometer arm. The resulting flower-shaped interference pattern is imaged with a CCD camera. An example pattern for a SPP with topological charge $m_l = 3$ is shown in Fig. 1(b).
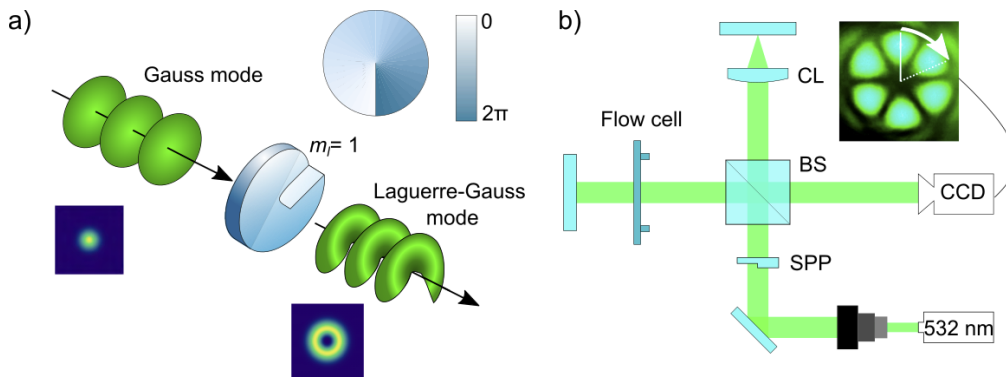
Fig. 1. SPP beam transformation and Michelson interferometer setup. a) Illustration of the transformation of a Gaussian TEM_{00} beam by a SPP into a Laguerre-Gaussian beam. b) Schematic of the Michelson interference setup. A 532 nm laser is first expanded by a beam expander to fully illuminate the spiral phase plate. In one arm of the Michelson interferometer a cylindrical lens (CL) turns the helicity of one arm. In the other arm a flow cell containing the sample is placed. A CCD camera detects the resulting interference pattern. The white arrow in the interference pattern indicates the rotation upon a phase shift in the beam path. Each arm of the interferometer spans about 30 cm.

As mentioned before, OAM beams have a distinct topological charge m_l, depending on the number of windings within one section of $\lambda \cdot m_l$ along the propagation direction [13]. As shown in Fig. 1(a), a SPP with one section is introducing a phase shift from 0 to 2π across the entire azimuthal angle θ of the SPP. This generates an OAM beam with $m_l = 1$. The presented interference pattern in Fig.1b results from OAM beams with $m_l = 3$. Figure 2 shows SPPs of higher order and the resulting OAM beams and interference patterns with topological charges $m_l = 2$, 3 and 6. If multiple sections introducing phase shifts from 0 to 2π are present within the same SPP and each section only spans, for example, 180° of the SPP as shown in the upper row for $m_l = 2$, the generated OAM beam is of a higher topological charge. The resulting interference pattern always has $2m_l$ number of maxima or flower petals. For higher orders more phase shifting sections are placed on the SPP. The higher the topological charge, the larger the central minimum of the mode profile and the diameter of the doughnut [21,55]. The experimentally obtained beam profiles are compared to simulated predictions and show identical intensity distributions. A detailed mathematical derivation and description of the resulting interference field of OAM beams can be found in literature [9,59].

The rotation of the interference pattern caused by a phase change in the optical path in one of the interferometer arms is directly proportional to a change in refractive index as shown in Eq. (2):

$$\theta_{rot} = \frac{360° d \Delta n}{\lambda m_l} \tag{2}$$

in which d is the optical path length in which the refractive index n changes and in our case the inner thickness of the flow cell. The wavelength of the laser λ is always constant. The smaller the topological charge, the larger the rotation of the individual petals [21,23]. In our experiments we measure concentration or temperature change, which is related to Δn, by measuring the rotation of the interference pattern. The interference patterns are analyzed automatically in an in-house developed analysis program which is further described in the Supporting Information and illustrated in Fig. S1.

Before applying the interferometer to refractive index measurements, we examined the fluctuations of the interference pattern without any sample present. Such fluctuations determine
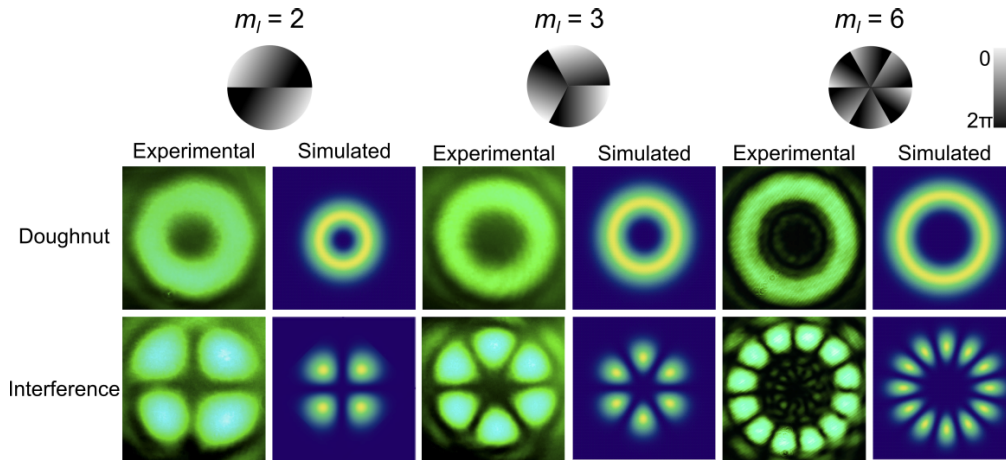
Fig. 2. SPPs generating OAM beams and interference patterns for $m_l = 2, 3$ and 6. For each phase plate with topological charge m_l the experimentally measured and simulated doughnut beam as well as the interference pattern of two beams with opposing m_l are shown.
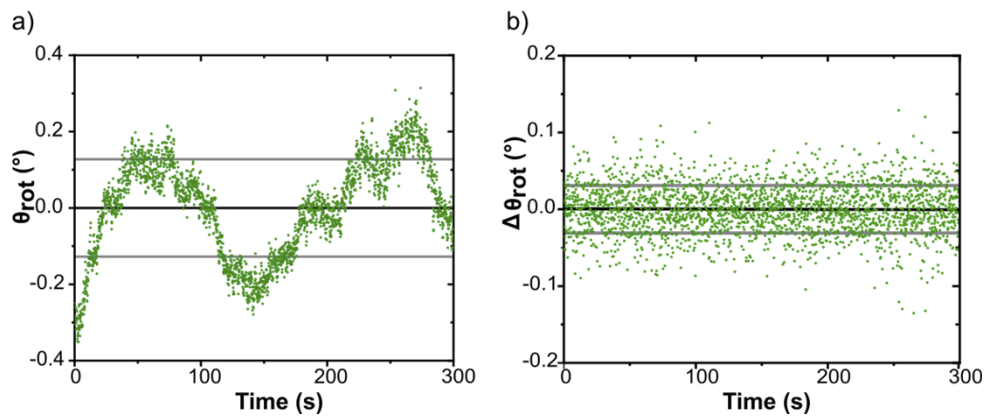

Fig. 3. Noise of the measured rotation angle over time of the interferometer. a) The interference pattern with no changes is recorded over 300 seconds. The grey bars indicate the standard deviation of $0.128°$. b) The change of rotation $\Delta\theta_{rot}$ is plotted. Again, the grey bars indicate the standard deviation of $0.03087°$.

the resolution of the setup and therefore need to be analyzed carefully. Figure 3 shows the rotation angle θ_{rot} measured over time. The measurement is conducted with a frame rate of 25 frames per second. We observe that fluctuations occur on two timescales; on the order of minutes and on the order of the acquisition frame rate. In Fig. 3(a), the slow component can be seen clearly. Fluctuations within a standard deviation of 0.128° are observed. The slow component has a period of more than 2 minutes and is caused by combination of environmental factors in the laboratory such as table vibrations, air flow or small temperature fluctuations. The fast component relates to the angle fluctuations measured from frame to frame. These fluctuations stem from the image acquisition noise. To distinguish this component more clearly, the change of the rotation angle $\Delta\theta_{rot}$ from frame to frame is plotted in Fig. 3(b). The standard deviation in this case is 0.0310°. A Fourier transform of Fig. 3(a) is included in the Supporting Information in Fig. S2. This 0.128° uncertainty over time in the rotation angle sets the limit of our sensitivity and corresponds to a change in the refractive index of $2.84 \cdot 10^{-7}$ RIU. This limit will be considered in the following measurements. Furthermore, the rotation angle θ_{rot} of the interference pattern is tracked frame-by-frame, using a CCD camera. For two consecutive images, the rotation angle θ_{rot} should thus be smaller than $360°/m_l$, with m_l being the topological charge. For $\theta_{rot} = 360°/m_l$ the interference pattern repeats itself. The frame rate of the CCD camera should thus be sufficient to resolve rotation angles $\theta_{rot} < 360°/m_l$.

4. Concentration measurements

In the first experiment, different NaCl and glucose concentrations are measured with two SPPs of $m_l = 6$ and $m_l = 3$. The liquid flow cell placed in the interferometer path is first filled with ultrapure water with a resistivity of 18.2 MΩ at 25 °C and a content of foreign matter less than 5 ppb, referred to as double distilled water (ddH$_2$O). A dilution series of NaCl was prepared ranging in concentration from 8 mM to 200 μM (further details are provided in the Materials and Methods section). Each solution is placed in a syringe, which is connected to the flow cell by a microfluidic channel. A syringe pump is used to minimize disturbances and allow a constant flow.

The results for the NaCl measurements are presented in Fig. 4. A photograph of the flow cell with the OAM beams and the interference pattern is shown in Fig. 4(a). The rotation angle θ_{rot} is measured in response to the solution exchange in the flow cell. The video acquisition begins 1 minute before the syringe pump is started. This is to ensure a long plateau with no pattern rotation and stable experimental conditions (see Fig. 4(b)). A selection of the measured curves is shown to enhance clarity. The liquid mixes with the ddH$_2$O in the flow cell, therefore the concentration of NaCl gradually increases, detectable by an onset of the flower pattern rotation. After the entire solution in the flow cell is exchanged the rotation stops and the interference pattern stays at a constant angle. This is again recorded for ∼ 1 minute to extract a stable angle value. As can be seen in Fig. 4(b), the turning slope is steeper for higher concentrations, since a faster pattern rotation is induced due to the higher amount of ions injected in the flow cell.

From the rotation we calculate a change in refractive index according to Eq. (2). In Fig. 4(c), the refractive index changes corresponding to different concentrations over several consecutive measurements is shown. A linear fit is provided and represents our data accurately. The change in refractive index and concentration can be directly correlated. Our results agree well with the data reported from Tan et al. [33]. A comparison between the fit for our own data with the empirical formula provided by Tan for the refractive index/concentration relationship of NaCl is shown in the Supporting Information in Fig. S3.

Additionally, concentration measurements are performed with glucose solutions as a sample in order to show the suitability of this method for non-ionic analytes. Glucose is of high biological relevance. For example, diabetes patients need to perform measurements several times during a
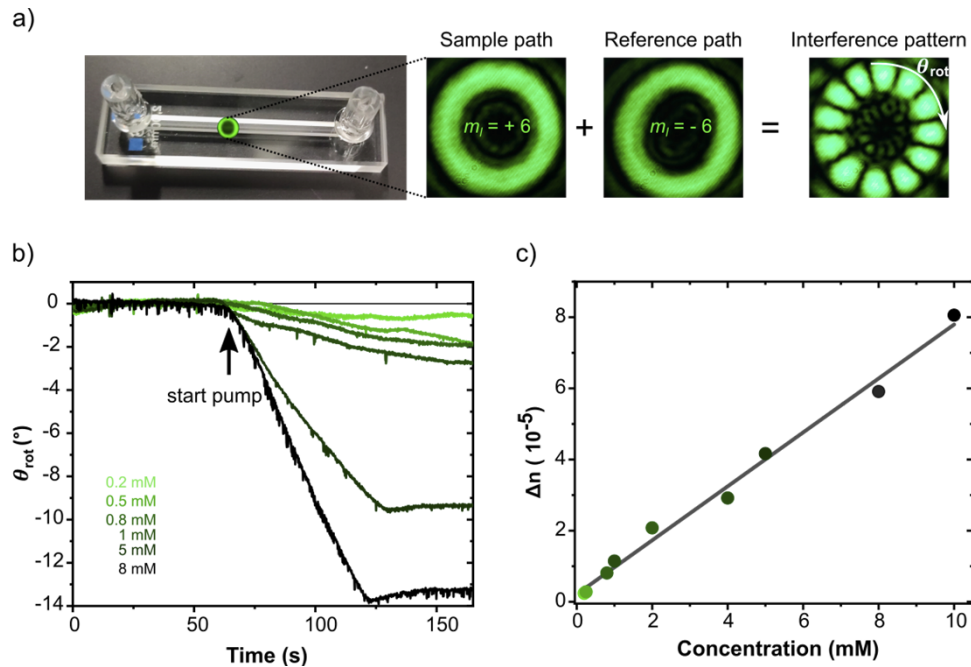
Fig. 4. Concentration measurements of NaCl in water and obtained changes of the refractive index. a) Photo of the flow cell and indication of the OAM beam on the flow cell. By combining the beam of the sample path and reference path, the interference pattern is created and detected on the CCD camera. The flower pattern rotates as liquid is pumped through the flow cell. b) Rotation angle θ_{rot} data over time for a selection of different NaCl solutions in the microfluidic chip. c) Linear correlation of the change in refractive index and the concentration of NaCl.

day. Currently, this is done by measuring glucose levels of blood samples but approaches to use other solutions such as the ocular fluid [60] are investigated.

A dilution series of aqueous glucose solutions was prepared ranging from 5 mM to 50 µM. Again, each of the solutions is connected to the microfluidic system via a syringe and then pumped inside the flow cell using a syringe pump. SPPs creating OAM beams with the topological charges $m_l = 3$ and $m_l = 6$ were used for the glucose measurements. For a smaller topological charge, the rotation for a phase shift is larger. However, this also means that fluctuations are dependent on the topological charge. Due to the relation described in Eq. (2), measurements with both SPPs can be plotted on the same axis when multiplying the rotation angle θ_{rot} with m_l. In Fig. 5(a), this product is plotted over time for different concentrations of glucose. The flow cell was first filled with ddH$_2$O. Shortly after starting the pump, a rotation of the interference pattern is visible, as shown in Fig. 5(a). After some time, a new plateau value is reached when the concentration is constant again. The average pattern position of the plateau is calculated and considered for the absolute value of the rotation. In Fig. 5(b), a linear fit is applied to the calculated change in refractive index values, which again is in very good agreement with literature [31,33]. Multiple measurements for the same concentrations were also performed to confirm the reproducibility of the measurements (Fig. 5(b)). The inset shows the smallest refractive index change values more clearly corresponding to the curves plotted in the inset in Fig. 5(a). The linear fit is also representing this data range very accurately. Like for the NaCl data the literature values are plotted and compared with the obtained results in the Supporting Information in Fig. S3.
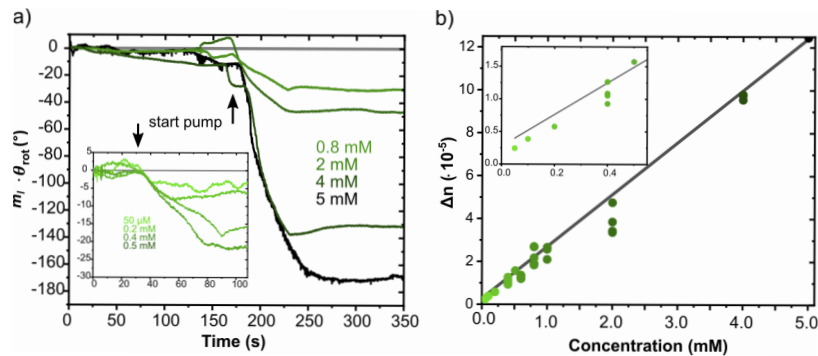
Fig. 5. Concentration measurements of glucose in water and obtained changes of the refractive index. a) Rotation angle θ_{rot} data scaled with topological charge m_l over time for a selection of glucose solutions in the microfluidic chip. Inset showing measurements of smaller concentration values. b) Linear correlation of the change in refractive index and the concentration of glucose. Inset showing data points at low concentration.

Summing up the results of this measurement series, changes in the refractive index down to 10^{-6} RIU can be detected non-invasively. This corresponds to a NaCl concentration of 200 µM or a glucose concentration of 50 µM. Considering our resolution limit of $2.84 \cdot 10^{-7}$ RIU, our resolution limit in NaCl concentration is 37 µM (or $2.195 \cdot 10^{-4}$ weight %) and for glucose 11 µM (or $2.115 \cdot 10^{-4}$ weight %). As mentioned before, this simple setup providing such resolutions could be of great applicability in biological sensing or screening. The glucose levels in the ocular fluid for a diabetes patient are at around 300 µM and for healthy patients at 160 µM [61], which lies well within the resolvable range of our measurement. In contrast to OAM interferometry, other methods with glucose sensors for more sensitive measurements would require fluorescent labelling [53]. Using a standard UV-Vis absorption spectrometer for measuring NaCl and glucose concentrations, we find that the smallest resolvable concentration is 10 mM, which is much higher than the lowest concentration that can be measured with the OAM interferometer (Supporting Information in Fig. S4).

5. Temperature measurements

So far, the application of OAM interferometry was demonstrated for measuring concentrations in the µM range. However, these measurements require that the measured analyte is known. The concentrations of different unknown analytes in a sample cannot be determined, since they would all contribute to a refractive index change. For more complex fluidic samples and mixtures, the OAM interferometer must be calibrated accordingly to account for all analytes present.

To address a more general experimental parameter, a second experiment was conducted using the OAM interferometer for temperature measurements of ultrapure water (ddH$_2$O). The refractive index of water is temperature dependent. The thermo-optic coefficient (TOC) dn/dT of ddH$_2$O is in the order of magnitude of 10^{-4} RIU/°C [62–66] and therefore well within our resolution range. To conduct the experiment, the ddH$_2$O is first heated and then allowed to cool down to room temperature. The process is monitored simultaneously with a high-resolution infrared camera to correlate the rotation angle change with the temperature change. Figure 6(a) shows the setup with the added IR camera for the concurrent control temperature measurement. A flow cell with a larger surface area is used to provide a reasonably large region of interest (ROI) for the IR camera measurement. This ROI has a diameter of 3 mm and is used for the evaluation of the sample temperature. It is located exactly at the laser position and therefore detects the same temperature change as the interferometer. The flow cell is clearly visible in
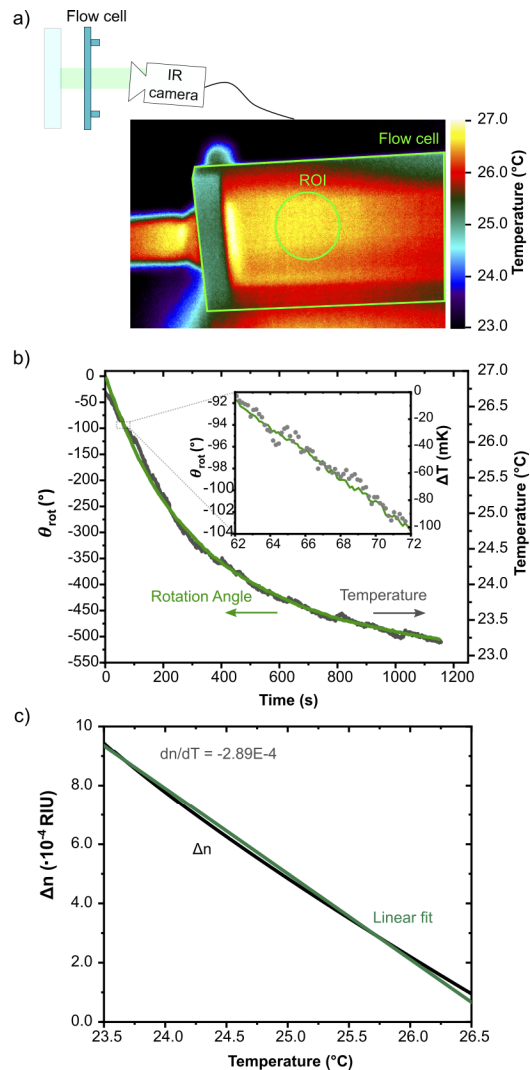
Fig. 6. Temperature measurements. a) An IR camera is introduced to track the change in temperature in the flow cell simultaneously. b) Measured rotation angle θ_{rot} and temperature over time as a sample of ddH$_2$O cools down. The inset shows a range of 10 s. The temperature scale is now in mK. c) Linear change in refractive index against temperature with the resulting dn/dT from a linear fit.

the IR camera recording. It can be seen that the liquid is warmest where it is injected, roughly in the center of the flow cell. The IR camera is also used to confirm that the laser itself does not heat the sample by itself. As the sample cools down to room temperature, a rotation of the interference pattern is observed. The temperature decrease due to convection and conduction is an exponential process over time which is described by Newton's law of cooling [67]. A mono-exponential fit describes the data with a R^2 value of 0.9992 (Fig. 6(b)). The rotation of

the interference pattern can perfectly be matched to the temperature decrease measured by the IR camera. Figure 6(b) shows an inset of the data where it becomes evident that this method is capable of measuring temperature in the mK range. Averaging over all performed measurements, the resulting slope is 7 mK/°. Considering our measurement resolution of the rotation angle θ_{rot} of 0.128°, the obtainable resolution for temperature measurements in our configuration is 890 µK. Considering a resolution of the rotation angle as theoretically determined by Verma and Yadav [26] of $\theta_{rot,min}$ of 0.0020°, the smallest resolvable temperature change could potentially reach 14 µK. The change of refractive index has been determined from the rotation angle using Eq. (2) and this value has been plotted against temperature in Fig. 6(c). A linear fit is used to describe this plot and the slope, calculated at - $2.89 \cdot 10^{-4}$ RIU/°C. This value of dn/dT is the aforementioned thermo-optic coefficient (TOC) of water. The TOC obtained in our measurement ranks within the same order of magnitude reported from other studies as shown in Table 1. However, these literature values were obtained from refractive index measurements using refractometers while controlling the temperature and were measured at different wavelengths [63,65] and temperature ranges [66], leading to the variation of about $1 \cdot 10^{-4}$ RIU/°C. The temperature control was only precise to about 1°C [63]. The value shown for Schiebener et al. [65] was given as a common result of comparing 12 literature values for several temperature ranges.

Table 1. Thermo-optic coefficient for water. Comparing the measured result to literature values in which the temperature was controlled and the refractive index was measured with a refractometer.

	OAM interferometry (Our work)	Subedi et al. [64]	Schiebener et al. [65]	Domenegueti et al. [66]	Kim et al. [63]
-dn/dT· 10^4 (RIU/°C)	2.89	1.85	2.0	2.0	0.8

It should be noted that the glass flow cell does not provide the ideal emissivity to measure temperature radiatively. Measurements in the mK range otherwise require much more complex equipment and for example, IR camera measurements are optimized for highly emissive surfaces. Therefore, with an OAM interferometer, we provide an alternative to measure temperature optically with remarkable resolution, especially for transmissive samples such as liquids in flow cells.

6. Discussion

In summary, we have shown that the interference of OAM beams offers a versatile method to measure changes in the refractive indices in the range of 10^{-6} RIU for extremely low concentration and temperature changes with high accuracy and reproducibility. To the best of our knowledge this is the first display of using a helical light mode interferometer to measure concentrations and temperature of liquids. Our experimental result for the dependence of the refractive index on the solution concentration are in excellent agreement with several previously published studies [31,33]. Temperature measurements are possible with mK accuracy and our extracted value for the TOC of water lies well within the range of literature values. We have analyzed the fluctuations measured in the interferometer and achieve a standard deviation of 0.128° of the rotation angle θ_{rot} translating into a resolution of $2.84 \cdot 10^{-7}$ RIU. These fluctuations may originate from changes of the refractive index of the ambient air due to temperature, pressure and humidity changes [68]. This is a common problem in interferometry [8] and could be mathematically compensated for. Placing the setup in a vacuum chamber could further decrease the fluctuations and improve the resolution. The measured signal is currently only segmented with a set threshold but no modulation or other signal post-processing methods are performed which could again increase the resolution of such measurements [8,39]. Instead of a CCD camera, position-sensitive devices or photodetectors could be used, which could potentially improve

the measurement accuracy and resolution of the system. Also, increasing the channel width or including several channels comparable to Ymeti et al. [69] could further improve the OAM interferometer performance. It should be noted that a change in temperature and concentration at the same time would simultaneously affect the refractive index of the sample. To avoid any crosstalk between these parameters, either the sample temperature or the concentration of the analyte was kept constant throughout our measurements. However, for specific applications, such as monitoring the progress of a chemical reaction, all experimental parameters affecting the refractive index (i.e. temperature, concentration, sample viscosity etc.) must be controlled or accounted for in the analysis. This, however, is not an issue specific for OAM interferometry, but a general requirement for refractive index measurements by other techniques as well.

OAM interferometry could find great application in microfluidic and lab-on-a-chip approaches as it enables the monitoring of concentration changes or gradients *in situ* on a μM scale as we have shown in a microfluidic cell. Temperature can also be monitored *in situ* on a mK scale, for example during chemical reactions. In pharmaceutical manufacturing, the close monitoring of such parameters is crucial [35]. Our OAM interferometer provides a simple and cheap method to measure changes in the refractive index with extremely high precision. It is not placed in a vacuum chamber or a clean room and can therefore be implemented into already existing experimental setups where fast, in-line monitoring of concentration or temperature is desirable.

Disclosures. The authors declare no conflicts of interest.

Data availability. Data underlying the results presented in this paper are not publicly available at this time but may be obtained from the authors upon reasonable request.

Supplemental document. See Supplement 1 for supporting content.

References

1. A. Michelson and E. W. Morley, "On the Relative Motion of the Earth and of the Luminiferous Ether," Am. J. Sci. **s3-34**(203), 333–345 (1887).
2. B. P. Abbott, R. Abbott, and T. D. Abbott, *et al.*, "Observation of Gravitational Waves from a Binary Black Hole Merger," Phys. Rev. Lett. **116**(6), 061102 (2016).
3. R. X. Adhikari, "Gravitational radiation detection with laser interferometry," Rev. Mod. Phys. **86**(1), 121–151 (2014).
4. J. Lawall and E. Kessler, "Michelson interferometry with 10 pm accuracy," Rev. Sci. Instrum. **71**(7), 2669–2676 (2000).
5. M. Pisani, "A homodyne Michelson interferometer with sub-picometer resolution," Meas. Sci. Technol. **20**(8), 084008 (2009).
6. R. Schödel, A. Yacoot, and A. Lewis, "The new mise en pratique for the metre — a review of approaches for the practical realization of traceable length metrology from $10-11$ m to $10+13$ m," Metrologia **58**(5), 052002 (2021).
7. T. Hausotte, B. Percle, U. Gerhardt, D. Dontsov, E. Manske, and G. Jäger, "Interference signal demodulation for nanopositioning and nanomeasuring machines," Meas. Sci. Technol. **23**(7), 074004 (2012).
8. Y.-S. Jang and S.-W. Kim, "Compensation of the refractive index of air in laser interferometer for distance measurement: A review," Int. J. Precis. Eng. Manuf. **18**(12), 1881–1890 (2017).
9. O. Emile and J. Emile, "Naked eye picometer resolution in a Michelson interferometer using conjugated twisted beams," Opt. Lett. **42**(2), 354–357 (2017).
10. M. W. Beijersbergen, R. P. C. Coerwinkel, M. Kristensen, and J. P. Woerdman, "Helical-wavefront laser beams produced with a spiral phase plate," Opt. Comm. **112**(5-6), 321–327 (1994).
11. M. Padgett and L. Allen, "Light with a twist in its tail," Contemp.Phys. **41**(5), 275–285 (2000).
12. L. Allen, M. W. Beijersbergen, R. J. Spreeuw, and J. P. Woerdman, "Orbital angular momentum of light and the transformation of Laguerre-Gaussian laser modes," Phys. Rev. A **45**(11), 8185–8189 (1992).
13. B. A. Knyazev and V. G. Serbo, "Beams of photons with nonzero projections of orbital angular momenta: new results," Phys.-Usp. **61**(5), 449–479 (2018).

14. O. Émile, C. Brousseau, J. Émile, and K. Mahdjoubi, "Energy and angular momentum transfers from an electromagnetic wave to a copper ring in the UHF band," C. R. Phys. **18**(2), 137–143 (2017).

15. S. W. Hell and J. Wichmann, "Breaking the diffraction resolution limitby stimulated emission:stimulated-emission-depletion fluorescence microscopy," Opt. Lett. **19**(11), 780 (1994).

16. M. J. Padgett, "Orbital angular momentum 25 years on [Invited]," Opt. Express **25**(10), 11265–11274 (2017).

17. Y. Shen, X. Wang, Z. Xie, C. Min, X. Fu, Q. Liu, M. Gong, and X. Yuan, "Optical vortices 30 years on: OAM manipulation from topological charge to multiple singularities," Light: Sci. Appl. **8**(1), 90 (2019).

18. Y. W. Huang, N. A. Rubin, A. Ambrosio, Z. Shi, R. C. Devlin, C. W. Qiu, and F. Capasso, "Versatile total angular momentum generation using cascaded J-plates," Opt. Express **27**(5), 7469–7484 (2019).

19. R. C. Devlin, A. Ambrosio, N. A. Rubin, J. P. B. Mueller, and F. Capasso, "Arbitrary spin-to–orbital angular momentum conversion of light," Science **358**(6365), 896–901 (2017).

20. R. Fickler, R. Lapkiewicz, W. N. Plick, M. Krenn, C. Schaeff, S. Ramelow, and A. Zeilinger, "Quantum Entanglement of High Angular Momenta," Science **338**(6107), 640–643 (2012).

21. E. Wisniewski-Barker, G. M. Gibson, S. Franke-Arnold, R. W. Boyd, and M. J. Padgett, "Mechanical Faraday effect for orbital angular momentum-carrying beams," Opt. Express **22**(10), 11690–11697 (2014).

22. N. Cvijetic, G. Milione, E. Ip, and T. Wang, "Detecting Lateral Motion using Light's Orbital Angular Momentum," Sci. Rep. **5**(1), 15422 (2015).

23. Q. Jia, X. Qiu, Z. Wu, W. Zhang, and L. Chen, "Transferring linear motion of an optical wedge to rotational frequency shift in an orbital angular momentum interferometer," Appl. Phys. Lett. **111**(9), 091102 (2017).

24. H. Lu, Y. Hao, C. Guo, X. Huang, H. Hao, D. Guo, H. Zhao, W. Tang, P. Wang, and H. Li, "Nano-Displacement Measurement System Using a Modified Orbital Angular Momentum Interferometer," IEEE J. Quantum Electron. **58**(2), 1–5 (2022).

25. Y. Ren, S. Qiu, T. Liu, and Z. Liu, "Compound motion detection based on OAM interferometry," Nanophotonics **11**(6), 1127–1135 (2022).

26. G. Verma and G. Yadav, "Compact picometer-scale interferometer using twisted light," Opt. Lett. **44**(14), 3594–3597 (2019).

27. A. Gatto, M. Tacca, F. Kéfélian, C. Buy, and M. Barsuglia, "Fabry-Pérot-Michelson interferometer using higher-order Laguerre-Gauss modes," Phys. Rev. D **90**(12), 122011 (2014).

28. S. Fürhapter, A. Jesacher, S. Bernet, and M. Ritsch-Marte, "Spiral interferometry," Opt. Lett. **30**(15), 1953 (2005).

29. A. Allocca, A. Gatto, M. Tacca, R. A. Day, M. Barsuglia, G. Pillant, C. Buy, and G. Vajente, "Higher-order Laguerre-Gauss interferometry for gravitational-wave detectors with in situ mirror defects compensation," Phys. Rev. D **92**(10), 102002 (2015).

30. B. Sorazu, P. J. Fulda, B. W. Barr, A. S. Bell, C. Bond, L. Carbone, A. Freise, S. Hild, S. H. Huttner, J. Jacarthur, and A. Strain, "Experimental test of higher-order Laguerre–Gauss modes in the 10 m Glasgow prototype interferometer," Class. Quantum Grav. **30**(3), 035004 (2013).

31. E. Misto, Purwandari, A. Supriyadi, L. Arkundato, B. E. Rohman, and Cahyono, "Analyses of Concentration and Wavelength Dependent Refractive Index of Sugar Solution Using Sellmeier Equation," J. Phys.: Conf. Ser. **1825**(1), 012030 (2021).

32. A. N. Bashkatov and E. A. Genina, "Water refractive index in dependence on temperature and wavelength: a simple approximation," in *Saratov Fall Meeting 2002: Optical Technologies in Biophysics and Medicine IV*, (SPIE, 2002), pp. 393–395.

33. C.-Y. Tan and Y.-X. Huang, "Dependence of Refractive Index on Concentration and Temperature in Electrolyte Solution, Polar Solution, Nonpolar Solution, and Protein Solution," J. Chem. Eng. Data **60**(10), 2827–2833 (2015).

34. J. G. Gardeniers and A. van den Berg, "Lab-on-a-chip systems for biomedical and environmental monitoring," Anal. Bioanal. Chem. **378**(7), 1700–1703 (2004).

35. B. Schreiber, C. Wacinski, and R. Chiarello, "Index of Refraction as a Quality Control Metric for Liquids in Pharmaceutical Manufacturing," Pharm. Eng. **33**, 1–7 (2013).

36. Y. Zhao, M. Dai, Z. Chen, X. Liu, M. S. A. Gandhi, Q. Li, and H. Y. Fu, "Ultrasensitive temperature sensor with Vernier-effect improved fiber Michelson interferometer," Opt. Express **29**(2), 1090–1101 (2021).

37. D. R. Vogus, V. Mansard, M. V. Rapp, and T. M. Squires, "Measuring concentration fields in microfluidic channels in situ with a Fabry-Perot interferometer," Lab Chip **15**(7), 1689–1696 (2015).

38. A. Crespi, Y. Gu, B. Ngamsom, H. J. Hoekstra, C. Dongre, M. Pollnau, R. Ramponi, H. H. van den Vlekkert, P. Watts, G. Cerullo, and R. Osellame, "Three-dimensional Mach-Zehnder interferometer in a microfluidic chip for spatially-resolved label-free detection," Lab Chip **10**(9), 1167–1173 (2010).

39. R. G. Heideman and P. V. Lambeck, "Remote opto-chemical sensing with extreme sensitivity: design, fabrication and performance of a pigtailed integrated optical phase-modulated Mach–Zehnder interferometer system," Sens. Actuators B Chem. **61**(1-3), 100–127 (1999).

40. J. Tian, Y. Lu, Q. Zhang, and M. Han, "Microfluidic refractive index sensor based on an all-silica in-line Fabry–Perot interferometer fabricated with microstructured fibers," Opt. Express **21**(5), 6633–6639 (2013).

41. T. Wei, Y. Han, Y. Li, H. L. Tsai, and H. Xiao, "Temperature-insensitive miniaturized fiber inline Fabry-Perot interferometer for highly sensitive refractive index measurement," Opt. Express **16**(8), 5764–5769 (2008).

42. S. Ghosh and B. M. A. Rahman, "Design of on-chip hybrid plasmonic Mach-Zehnder interferometer for temperature and concentration detection of chemical solution," Sens. Actuators B Chem. **279**, 490–502 (2019).

43. G. H. Cross, A. A. Reeves, S. Brand, J. F. Popplewell, L. L. Peel, M. J. Swann, and N. J. Freeman, "A new quantitative optical biosensor for protein characterisation," Biosens. Bioelectron. **19**(4), 383–390 (2003).

44. D. J. Bornhop, J. C. Latham, A. Kussrow, D. A. Markov, R. D. Jones, and H. S. Sorensen, "Free-solution, label-free molecular interactions studied by back-scattering interferometry," Science **317**(5845), 1732–1736 (2007).

45. A. Brandenburg, "Differential refractometry by an integrated-optical Young interferometer," Sens. Actuators B Chem. **39**(1-3), 266–271 (1997).

46. K. E. You, N. Uddin, T. H. Kim, Q. H. Fan, and H. J. Yoon, "Highly sensitive detection of biological substances using microfluidic enhanced Fabry-Perot etalon-based optical biosensors," Sens. Actuators B Chem. **277**, 62–68 (2018).

47. A. Ymeti, J. S. Kanger, R. Wijn, P. V. Lambeck, and J. Greve, "Development of a multichannel integrated interferometer immunosensor," Sens. Actuators B Chem. **83**(1-3), 1–7 (2002).

48. H. Sobral and M. Pena-Gomar, "Determination of the refractive index of glucose-ethanol-water mixtures using spectroscopic refractometry near the critical angle," Appl. Opt. **54**(28), 8453–8458 (2015).

49. C. Wu, M. L. Tse, Z. Liu, B. O. Guan, A. P. Zhang, C. Lu, and H. Y. Tam, "In-line microfluidic integration of photonic crystal fibres as a highly sensitive refractometer," Analyst **139**(21), 5422–5429 (2014).

50. F. N. D. D. Pereira and A. C. H. Hallett, "A New Double Beam Optical Lever Refractometer and the Variation of the Refractive Index of NaCl with Temperature," Rev. Sci. Instrum. **42**(4), 490–493 (1971).

51. D. P. Duarte, R. N. Nogueira, and L. B. Bilro, "A low-cost liquid refractive index sensor based on plastic optical fibre and CCD array," Meas. Sci Technol. **31**(4), 047001 (2020).

52. A. Paar, "The universal refractometer 1-7" (Anton Paar, 2018), retrieved 05 April, 2022.

53. Y. Kostov, X. Ge, G. Rao, and L. Tolosa, "Portable system for the detection of micromolar concentrations of glucose," Meas. Sci. Technol. **25**(2), 025701 (2014).

54. K. Sueda, G. Miyaji, N. Miyanaga, and N. Nakatsuka, "Laguerre-Gaussian beam generated with a multilevel spiral phase plate for high intensity laser pulses," Opt. Express **12**(15), 3548 (2004).

55. M. Cano-Garcia, X. Quintana, J. M. Oton, and M. A. Geday, "Dynamic multilevel spiral phase plate generator," Sci. Rep. **8**(1), 15804 (2018).

56. S. S. R. Oemrawsingh, J. A. W. van Houwelingen, E. R. Eliel, J. P. Woerdman, E. J. K. Verstegen, J. G. Kloosterboer, and G. W. 't Hooft, "Production and characterization of spiral phase plates for optical wavelengths," Appl. Opt. **43**(3), 688–694 (2004).

57. P. Kumar and N. K. Nishchal, "Modified Mach-Zehnder interferometer for determining the high-order topological charge of Laguerre-Gaussian vortex beams," J. Opt. Soc. Am. A **36**(8), 1447–1455 (2019).

58. P. Kumar and N. K. Nishchal, "Self-referenced interference of laterally displaced vortex beams for topological charge determination," Opt. Comm. **459**, 125000 (2020).

59. J. Guo, B. Guo, R. Fan, W. Zhang, Y. Wang, L. Zhang, and P. Zhang, "Measuring topological charges of Laguerre–Gaussian vortex beams using two improved Mach–Zehnder interferometers," Opt. Eng. **55**(3), 035104 (2016).

60. D. Bruen, C. Delaney, L. Florea, and D. Diamond, "Glucose Sensing for Diabetes Monitoring: Recent Developments," Sensors **17**(8), 1866 (2017).

61. J. Zhang, W. Hodge, C. Hutnick, and X. Wang, "Noninvasive diagnostic devices for diabetes through measuring tear glucose," JDST **5**, 166–172 (2011).

62. E. Kendir and Ş Yaltkaya, "Effect of temperature and wavelength on the refractive index of water: a fiber-optic sensor application," Indian J. Phys. **96**(4), 1247–1252 (2022).

63. Y. H. Kim, S. J. Park, S.-W. Jeon, S. Ju, C.-S. Park, W.-T. Han, and B. L. Lee, "Thermo-optic coefficient measurement of liquids based on simultaneous temperature and refractive index sensing capability of a two-mode fiber interferometric probe," Opt. Express **20**(21), 23744 (2012).

64. D. P. Subedi, D. R. Adhikari, U. M. Joshi, H. N. Poudel, and B. Niraula, "Study of temperature and concentration dependence of refractive index of liquids using a novel technique," Kathmandu Uni. J. Sci. Engineer. and Technol. **2**, 1–7 (2006).

65. P. Schiebener, J. Straub, J. M. H. Levelt Sengers, and J. S. Gallagher, "Refractive index of water and steam as function of wavelength, temperature and density," J. Phys. Chem. Ref. Data **19**(3), 677–717 (1990).

66. J. F. Domenegueti, A. A. Andrade, V. Pilla, and S. C. Zilio, "Simultaneous measurement of thermo-optic and thermal expansion coefficients with a single arm double interferometer," Opt. Express **25**(1), 313–319 (2017).

67. U. Grigull, "Newton's temperature scale and the law of cooling," Wärme- und Stoffübertragung **18**(4), 195–199 (1984).

68. R. Schödel, A. Walkov, M. Voigt, and G. Bartl, "Measurement of the refractive index of air in a low-pressure regime and the applicability of traditional empirical formulae," Meas. Sci. Technol. **29**(6), 064002 (2018).

69. A. Ymeti, J. S. Kanger, J. Greve, G. A. Besselink, P. V. Lambeck, R. Wijn, and R. G. Heideman, "Integration of microfluidics with a four-channel integrated optical Young interferometer immunosensor," Biosens. Bioelectron. **20**(7), 1417–1421 (2005).